RSC Advances

PAPER

View Article Online
View Journal | View Issue

Cite this: *RSC Adv.*, 2022, **12**, 17312

Highly sensitive and convenient aptasensor based on Au NPs@Ce-TpBpy COF for quantitative determination of zearalenone†

Zhixiong Chen, Meng Yang, Ziying Li, Wenchun Liao, Bengqi Chen, Tong Yang, Rong Hu, Yunhui Yang* and Shuang Meng*

In this work, an aptasensor based on a portable U-disk electrochemical workstation in combination with a screen-printed electrode (SPE) is demonstrated for the quantitative determination of zearalenone (ZEN). The aptamer is immobilized on Au NPs@Ce-TpBpy COF (Covalent organic frameworks), which is modified on the surface of glassy carbon electrode. ZEN specifically binds to ZEN aptamer, which hinders the electron transfer and decreases the catalytic current of Au NPs@Ce-TpBpy COF for the reduction of hydrogen peroxide, measured by chronoamperometry (i–t). The quantitative detection of ZEN toxin is realized by a decrease of the catalytic current (ΔI). Under the optimal experimental conditions, the aptamer sensor exhibited excellent sensitivity, selectivity, reproducibility. A wide linear range of 1 pg mL^{-1}–10.0 ng mL^{-1} with a detection limit of 0.389 pg mL^{-1} (at 3σ) was obtained. The linear equation is $\Delta I = 0.401 \lg c + 1.948$ with a correlation coefficient of 0.9906. The recovery is in the range of 93.0–104.7% for the cornflour samples. The proposed method offers a new strategy for the rapid, inexpensive, and real-time detection of ZEN.

Received 31st March 2022
Accepted 26th May 2022

DOI: 10.1039/d2ra02093a

rsc.li/rsc-advances

Introduction

Zearalenone (ZEN), also known as F-2 toxin,[1–3] is an estrogenic mycotoxin commonly found in cereals, corn, and wheat.[4] Zearalenone and its derivatives have a significant effect on estrogen levels and the reproductive system. It causes some fertility problems, leads to miscarriage, the stillbirth of livestock or people, and reduces fertility.[5–9] Therefore, it is urgent to develop a highly sensitive and specific detection method to monitor the zearalenone levels in food to ensure food quality and safety.

At present, the commonly used technologies for zearalenone detection are high-performance liquid chromatography (HPLC),[10] enzyme-linked immunosorbent assay (ELISA),[11] and liquid chromatography-mass spectrometry (LC-MS),[12] electrochemical.[13] These technologies have satisfactory sensitivity, selectivity, and accuracy. However, HPLC and LC-MS are tedious, expensive, and time-consuming. ELISA is unstable in a harsh environment and shows false-positive results, besides high cost, the pre-processing time is more troublesome and cannot meet the needs of on-site real-time detection. Recently, mimetic peroxidase nanoparticles are used as catalysts for signal amplification,[14,15] the electrochemical detection performance was improved by modification these materials.[16,17]

Covalent organic frameworks (COFs) are emerging as a new class of porous solids with rigid and diversified structures, permanent porosity,[18] high surface area,[19] high thermal and chemical stability, tunable pore size, and low framework density. Owing to these structural features, COFs with adjustable features have been widely applied in different research areas, such as clean energy storage, molecular separations, photoelectric materials, and molecular motors. More recently, intensive efforts have been devoted to developing catalytic active COFs materials with a potential application in biosensors.[20,21] 2,2-Bipyridine compounds have been chosen as monomers for the synthesis of Ce-TpBpy COF.[22] The utilization of 2,2-bipyridine as an active site for constructing a stable framework prevents the leaching of rare-earth elements such as cerium. In addition, porous organic structures render the active sites isolated from each other, thus active centers are accessible to reactants.

This concept is exemplified in this study, by the targeted synthesis of Au NPs@Ce-TpBpy COF composite. Our previously reported strategy[23] has shown that Re-TpBpy COF structures were synthesized by 2,2-bipyridine and 1,3,5-triformyl phloroglucinol (Tp) under ionothermal conditions with high surface areas and tunable pore sizes. Subsequently, the Au NPs@Ce-TpBpy COF composite was successfully synthesized. An aptasensor was designed using a screen-printed electrode (SPE) and U-disk electrochemical workstation. The quantitative detection of zearalenone toxin was carried out by measuring the decreasing

College of Chemistry and Chemical Engineering, Yunnan Normal University, Kunming, 650500, China. E-mail: yyhui2002@aliyun.com; ms19880719@126.com; Fax: +86 871 65941086

† Electronic supplementary information (ESI) available. See https://doi.org/10.1039/d2ra02093a

catalytic current (ΔI). Furthermore, this method offers a new strategy for the rapid and inexpensive detection of ZEN.

Experimental section

Reagents and apparatus

Tris (hydroxymethyl) aminomethane, 30% hydrogen peroxide (H_2O_2), hexamethylenetetramine ($C_6H_{12}N_4$), phloroglucinol ($C_6H_6O_3$), trifluoroacetic acid (CF_3COOH), 1,3,5-triformylphloroglucinol, 2,2-bipyridine-5,5-diamine, *N*,*N*-dimethylacetamide, *o*-dichlorobenzene, tetrahydrofuran (THF), dichloromethane, chloroauric acid ($HAuCl_4$), 3,3,5,5-tetramethylbenzidine (TMB) and β-Mercaptoethanol (MCH) were purchased from Sigma-Aldrich (USA). Zearalenone toxin was bought from Shanghai Yuanye Biotechnology Co., Ltd (Shanghai, China). ZEN aptamer chain (5′ to 3′): AGCAGCACAGAGGTCAGATGTCATCATCATCA TCATCATCATCTATGGTATCATCATCATCATCATCATCTGTAAT GCATCATGCCTATGCGTGCTATCCGTGATTTTT-C6-SH (ref. 24) was synthesized by Bioengineering (Shanghai, China). Screen-printed electrodes (SPE) were purchased from Yum Instruments (Guangzhou, China). The chemical reagents and drugs were used directly without purification. All electrochemical measurements were carried out on U-disk electrochemical workstation (Sensit Smart, PalmSens BV). FTIR spectra (KBr) were recorded on Nicolet IS50 Fourier transform infrared spectrometer (FTIR). N_2 adsorption–desorption isotherms and pore size distributions were obtained at 77 K using an Autosorb iQ2 absorptiometer, Quantachrome Instrument. Transmission Electron Microscope (TEM) analysis was carried out on JEOL JEM 2100. The X-ray photoelectron spectroscopy (XPS) spectra were collected on K-Alpha+. The diffraction of X-rays (XRD) spectra were collected on Rigaku miniflex 600.

Synthesis of TpBpy COF

TpBpy COF were synthesized following the previous literature.[22] In brief, 1, 3, 5-triformylphloroglucinol (Tp) (25.2 mg) and 2, 2′-bipyridine-5, 5′-diamine (Bpy) (33.5 mg) were added to a pyrex tube (o. d. × i. d. = 16 × 12 mm^2 and length 18 cm) and dissolved in the mixture of 1.8 mL of dimethylacetamide (DMAc), 0.6 mL of *o*-dichlorobenzene (*o*-DCB) and 0.24 mL of 6.0 M aqueous acetic acid (AcOH). The reaction mixture was sonicated for 15 min to obtain a homogenous dispersion. The tube was flash-frozen in a liquid N_2 bath (77 K), degassed by three freeze–pump–thaw cycles, and flame sealed. Then, the mixture was heated at 120 °C and left undisturbed for 3 days, yielding a dark-red solid. The tube was broken at the neck, the product was isolated by filtration and washed with DMAc, water, and acetone. The collected powder was immersed in acetone for 12 h and the activation solvent was replenished three times. Finally, the product was dried at 100 °C under vacuum for 24 h to obtain the as-synthesized TpBpy COF (yield: 75%).

Synthesis of Ce-TpBpy COF

TpBpy COF (100 mg) and cerium nitrate hexahydrate (161 mg) were mixed in 20 mL methanol (MeOH). The mixture was refluxed for 24 h under N_2. The resultant red powder was washed with MeOH three times and collected by vacuum filtration. Finally, the product was dried at 80 °C in a vacuum oven for 12 h.

Synthesis of gold nanoparticles

Nano-gold sol was synthesized according to the method described in the literature.[25] Briefly, 50 mL of ultra-pure water was added to the round-bottom flask and 0.5 mL of 1% $HAuCl_4$ was added, stirred, and heated to boiling. 1.75 mL of 1% tri-sodium citrate was added, stirred, and heated for 20 min. The product was cooled to room temperature and the obtained wine-red nano-gold sol was stored at 4 °C.

Synthesis of Au NPs@Ce-TpBpy COF

Ce-TpBpy COF (50 mg) solid powder was dissolved in 25 mL deionized water. After ultrasonication, 15 mL of the nano-gold sol was added dropwise. The mixture was stirred at room temperature in dark for 48 h. The resultant product was centrifuged and washed with deionized water, and vacuum dried.

Construction of zearalenone aptamer sensor

10.4 mg mL^{-1} of Au NPs@Ce-TpBpy COF dispersion and 0.5% chitosan were mixed at a volume ratio of 1 : 1.5. Then, 6 μL of the mixture was dripped onto the surface of the screen-printed electrode as the substrate and dried at room temperature. Next, 6 μL of 1 μmol L^{-1} of ZEN aptamer was dripped on the surface of the screen-printed electrode. The aptamer chain was immobilized to Au NPs@Ce-TpBpy COF through Au–SH bond by incubating at 37 °C for 100 min. The electrode surface was washed three times with 0.2 M Tris acetic acid buffer solution (pH 7.0) to remove the weakly bound or unbound aptamer chains. 6 μL of 1% β-mercaptoethanol (MCH) was dripped and incubated at 37 °C for 30 min to block the non-specific binding site. The electrode surface was washed three times with 0.2 M Tris acetic acid buffer solution (pH 7.0) to remove excess MCH. Thus, the aptamer sensor was constructed.

The catalytic current for hydrogen peroxide reduction was measured by chronoamperometry (*i*–*t*) in 0.2 M Tris acetic acid buffer (pH 7.0). ZEN specifically binds to ZEN aptamer, hinders the electron transfer, and reduces the catalytic current of Au NPs@Ce-TpBpy COF for the reduction of hydrogen peroxide, the current decreases with the increase of ZEN concentration in the solution. The quantitative detection of ZEN toxin was carried out by measuring the decreasing catalytic current. The principle of the zearalenone aptasensor is shown in Scheme 1.

The detection method of aptasensor

Chronoamperometric method was used to detect the reduction current of hydrogen peroxide catalyzed by Au NPs@Ce-TpBpy COF in 0.2 M Tris acetic acid buffer solution (pH 7.0) at −0.6 V potential. Briefly, after the background current was stabilized (it takes about 20 s), H_2O_2 was added into the buffer to get final concentration of 0.1 mol L^{-1} and the catalytic current of Ce-TpBpy COF to the reduction of H_2O_2 (current change before and after H_2O_2 added) was recorded. The current

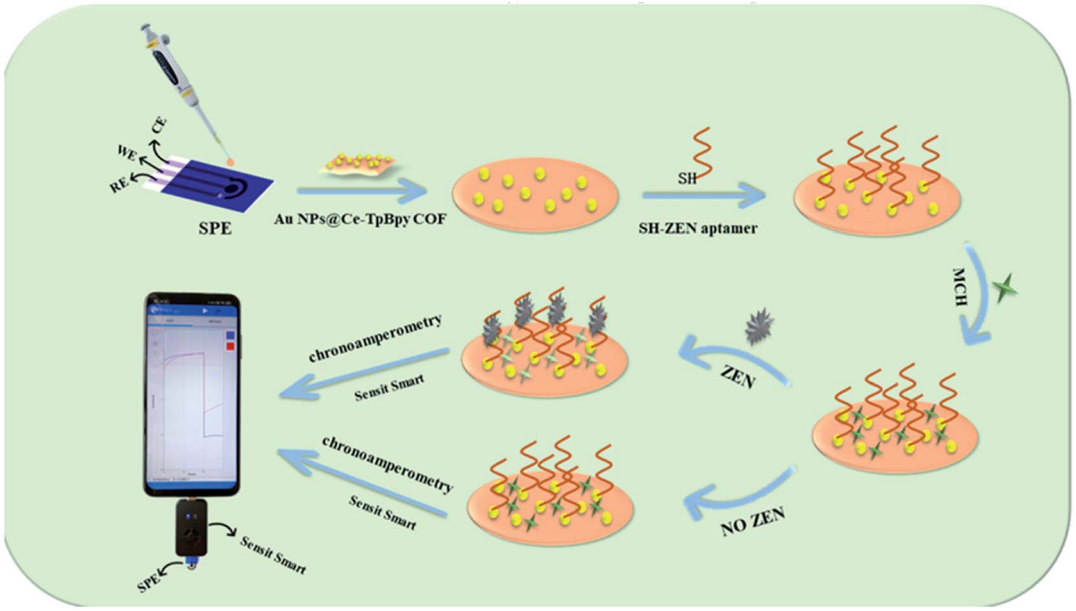

Scheme 1 Preparation process of ZEN aptasensor.

difference ΔI (the difference of response current without and with ZEN) was calculated as response signal.

Results and discussion

FTIR characterization of materials of TpBpy COF and Ce-TpBpy COF

The synthesized TpBpy COF and Ce-TpBpy COF were characterized by Fourier transform infrared (FTIR) spectroscopy and results are shown in Fig. 1. Strong IR peaks, corresponding to the stretching vibrations of the keto-form are observed at 1607 cm^{-1} (C═O). The broadened C–N peak at 1248 cm^{-1} reveals a slight red shift, indicative of the formation of Ce–N bonds in the polymer.

X-ray diffraction (XRD) characterization of TpBpy COF and Ce-TpBpy COF

In this experiment, TpBpy COF was prepared by a Schiff base condensation reaction, as shown in Fig. 2, and the X-ray diffraction results were consistent with ref. 22. The XRD patterns of TpBpy indicate a highly intense peak at $2\theta = 3.6°$ corresponding to the (100) plane reflections, with minor peaks at 6.0 and 25.1–28.6°. The strong peak reduction of Ce-TpBpy COF $2\theta = 3.6°$ is due to the fact that the doping of Ce element affects the crystal structure.

X-ray photoelectron spectroscopy (XPS) of Ce-TpBpy COF

In this experiment, the XPS of Ce-TpBpy COF was further determined, and the peaks of cerium ions Ce $3d_{3/2}$ and Ce $3d_{5/2}$ were observed in the XPS spectrum of Ce 3d (Fig. 3). The partial peak fitting of Ce $3d_{3/2}$ and Ce $3d_{5/2}$ regions found that they contain Ce^{3+} and Ce^{4+}, as shown in Fig. 3B, the binding energies are 905.73 eV, 900.04 eV, 887.12 eV and 881.54 eV are Ce^{4+} 3d energy levels and the content is 45.7%; the binding energy is

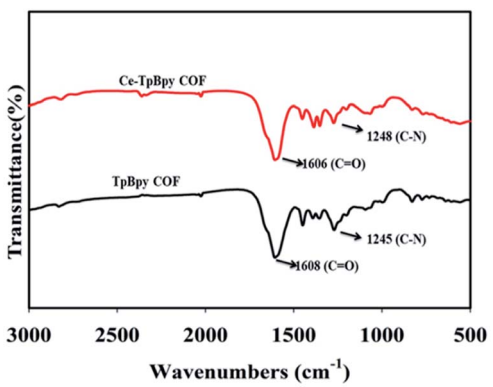

Fig. 1 FTIR spectra of TpBpy COF (black) and Ce-TpBpy COF (red).

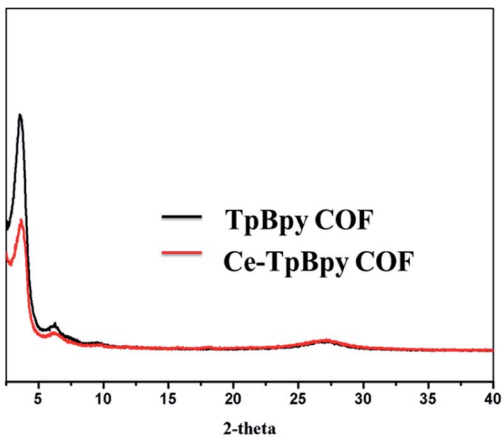

Fig. 2 XRD characterization of TpBpy COF (black) and Ce-TpBpy COF (red).

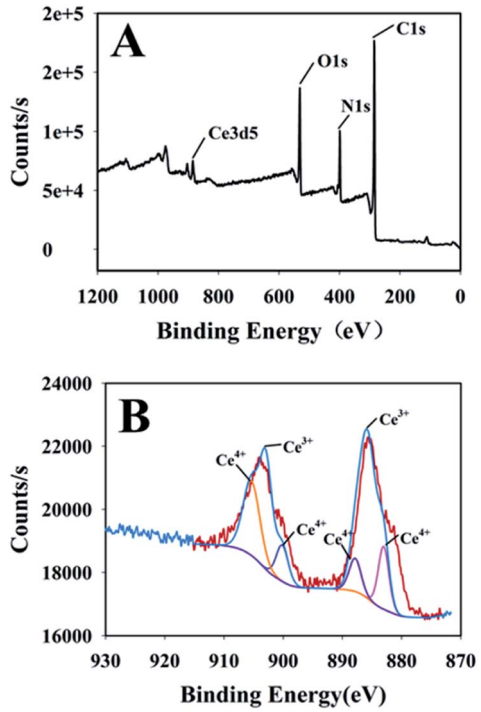

Fig. 3 XPS spectrum of Ce-TpBpy COF (A) and Ce 3d in Ce-TpBpy COF (B).

903.23 eV and 884.6 eV are Ce^{3+} 3d energy levels, and the content is 55.3%. The content of Ce^{3+} is higher, indicating that the activity of Ce-TpBpy COF-like peroxidase is higher.

Microstructure characterization of TpBpy COF, Ce-TpBpy COF and Au NPs@Ce-TpBpy COF

The morphology of TpBpy COF, Ce-TpBpy COF and Au NPs@Ce-TpBpy COF composite is characterized by transmission electron microscopy (Fig. 4). The TEM images indicate that TpBpy COF shows predominant sheet-like, it is observed that the gold nanoparticles are uniformly dispersed on the covalent organic frameworks.

N_2 adsorption–desorption isotherms curve of TpBpy COF and Ce-TpBpy COF

N_2 adsorption isotherms are measured at 77 K to investigate the porosity of TpBpy COF and Ce-TpBpy COF (Fig. 5). As indicated in Fig. 5, both materials show type I isotherms featured by a sharp uptake at the low-pressure region. By applying the Brunauer–Emmett–Teller (BET) model to the low-pressure region of the isotherms, the surface areas are 1631.2 $m^2\ g^{-1}$ and 1191.5 $m^2\ g^{-1}$. This phenomenon may have resulted from the occupancy of partial pore spaces in Ce-TpBpy COF by $Ce(NO)_3$ moieties. Notably, the BET surface area of Ce-TpBpy COF is still relatively high and the porous structure is well preserved. Therefore, high accessibility of the Ce active sites in the TpBpy COF channels is ensured. The pore size distributions of TpBpy COF and Ce-TpBpy COF are calculated by the non-local density functional theory (NLDFT) method. These products display the main pore size distribution in the range of 0.5 nm and 2.3 nm.

AC impedance characterization of the electrode assembly process

Electrochemical impedance spectroscopy (EIS) was used to characterize the surface modification process of the electrode.[26] The Randles circuit is shown in the inset of Fig. 6, where $R1$ is the solution resistance, $Q1$ is the capacitance, $R2$ is the membrane resistance, and $W1$ is the Warburg impedance. The diameter of the semi-circle is determined by the simulation results, the initial value of the semi-circle is determined as $Z' = 0$, and the size of the semi-circle is compared to achieve the process of characterizing the impedance change. As shown in Fig. 6, curve a is the impedance curve of bare SPE with an impedance of $R_{ct} = 4300\ \Omega$, curve b shows the impedance curve of the bare SPE modified by Au NPs@Ce-TpBpy COF. Owing to the good conductivity of Au NPs@Ce-TpBpy COF, the impedance of TpBpy COF reduced to $R_{ct} = 3750\ \Omega$. Curve c shows the

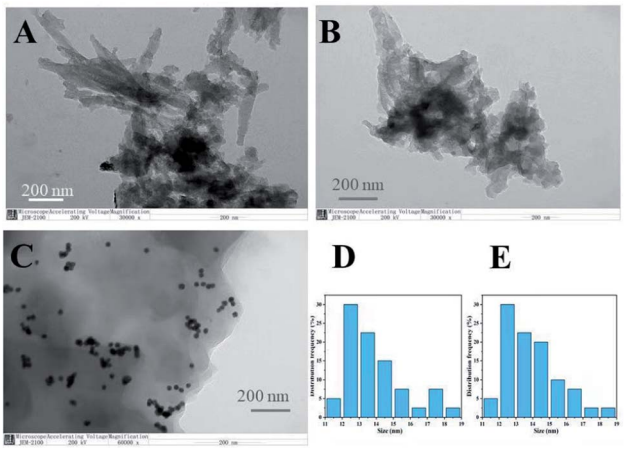

Fig. 4 TEM images of TpBpy COF (A), Ce-TpBpy COF (B) and Au NPs@Ce-TpBpy COF (C) and the size distribution of Au NPs before (D) and after (E) the decoration of Ce-TpBpy COF.

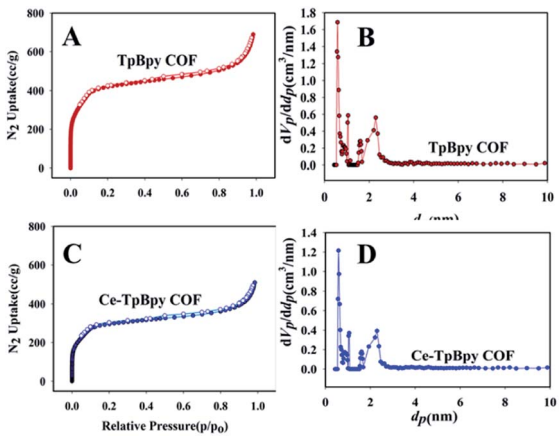

Fig. 5 N_2 adsorption–desorption isotherms curves of TpBpy COF (A) and Ce-TpBpy COF (C); main pore size distribution of TpBpy COF (B) and Ce-TpBpy COF (D).

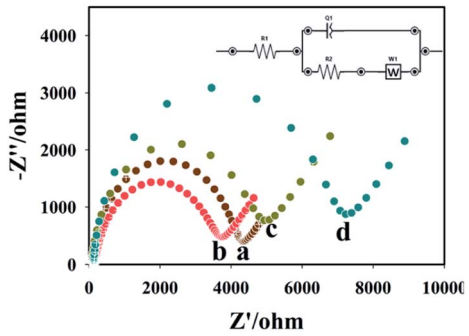

Fig. 6 Characterization of electrochemical impedance spectroscopy of aptamer sensor assembly (a) bare SPE, (b) Au NPs@Ce-TpBpy COF/CHIT/SPE, (c) SH-ZEN aptamer/Au NPs@Ce-TpBpy COF/CHIT/SPE, and (d) ZEN/SH-ZEN aptamer/Au NPs@Ce-TpBpy COF/CHIT/SPE.

impedance curve of ZEN aptamer/Au NPs@Ce-TpBpy COF/SPE, indicating the increased impedance to R_{ct} = 5200 Ω. These results indicate the non-conducting nature of aptamers, hence, the successful assembly of ZEN aptamer on the surface of the electrode. Curve *d* is the impedance diagram of ZEN/ZEN aptamer/Au NPs@Ce-TpBpy COF/SPE and it shows that the impedance increase to R_{ct} = 7500 Ω. This result indicates that ZEN aptamer has successfully captured ZEN.

Experimental feasibility analysis

To verify the feasibility of the experimental design, the catalytic ability of TpBpy COF and Ce-TpBpy COF for the reduction of hydrogen peroxide is studied. The electrochemical signals change when ZEN is introduced to the system (Fig. 7). Fig. 7A shows that the catalytic ability of the Ce doped TpBpy COF significantly improved for the reduction of hydrogen peroxide. After Au NPs were doped onto Ce -TpBpy COF, the catalytic current improved further, indicating Au NPs have synergistic effect with Ce-TpBpy COF to the reduction of H_2O_2. Fig. 7B shows the catalytic current of Ce-TpBpy COF for hydrogen peroxide is higher without ZEN in the system. However, when ZEN is introduced to the system, the catalytic current decreases. This shows that the proposed scheme is reasonable and feasible.

Optimization of the experimental conditions

To achieve ideal analytical performance, the experimental conditions are optimized.

Effect of pH on the current response

pH is an important factor that affects the reduction of hydrogen peroxide, catalyzed by Au NPs@Ce-TpBpy COF. The current response ΔI is determined by changing the pH of the buffer solution ($\Delta I = I_0 - I_x$) where I_0 is the current of the blank solution, I_x is the current of the solution with target ZEN. Change the pH value of the buffer solution (pH is 4, 5, 6, 7, 8, 9), and measure the current response ΔI value at different pH values. As shown in Fig. 8A, with the increasing pH, the current response of the aptamer sensor increases and reaches the highest at pH 7.0. After

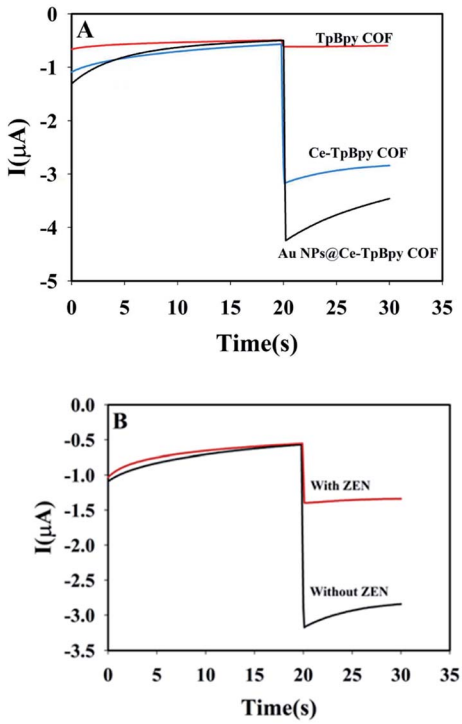

Fig. 7 Experimental feasibility analysis. (A) The catalytic current of TpBpy COF/CHIT/SPE, Ce-TpBpy COF/CHIT/SPE and Au NPs/Ce-TpBpy COF/CHIT/SPE for the reduction of hydrogen peroxide. (B) The catalytic current of SH-ZEN aptamer/Au NPs@Ce-TpBpy COF/CHIT/SPE and ZEN/SH-ZEN aptamer/Au NPs@Ce-TpBpy COF/CHIT/SPE for the reduction of hydrogen peroxide.

that, the current response decreases. Therefore, in the follow-up study, pH 7.0 was selected as the optimal pH value.

Effect of ZEN incubation time on the response current

The effect of the incubation time of ZEN on the current response was investigated experimentally. The pH of the buffer was kept at 7.0. The current response value ΔI of the aptamer

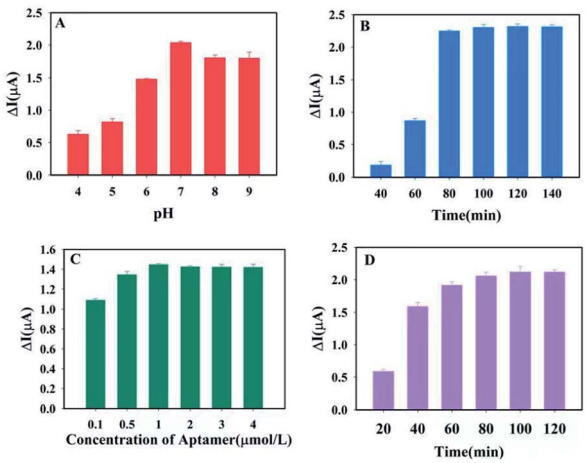

Fig. 8 Optimization of the conditions buffer pH (A), incubation time of ZEN (B), ZEN aptamer concentration (C), and incubation time of ZEN aptamers (D).

sensor was investigated when the incubation time was 40 min, 60 min, 80 min, 100 min, 120 min, and 140 min, respectively. Results as shown in Fig. 8B. With the increase of incubation time, ΔI gradually increased and then remained stable. The highest value of ΔI was observed at an incubation time of 100 min. Then, with the further increase of the incubation time, a slight change in ΔI was observed, indicating that the binding of ZEN to the aptamer chain reached the maximum at 100 min. Therefore, the optimal incubation time of ZEN was selected as 100 min in the follow-up study.

Effect of ZEN aptamer concentration on the response current

The concentration of ZEN aptamers is critical for the construction of the sensor. In order to study the effect of ZEN aptamer concentration on the sensor current response, other experimental conditions were fixed unchanged, the pH of the buffer was kept at 7.0, and the ZEN incubation time was 100 min. The concentrations of ZEN aptamers were set as 0.1 μmol L^{-1}, 0.5 μmol L^{-1}, 1 μmol L^{-1}, 2 μmol L^{-1}, 3 μmol L^{-1}, 4 μmol L^{-1}, and then the current response ΔI was measured. As shown in Fig. 8C, as the concentration of ZEN aptamer chains increases, ΔI gradually increases and then remains stable. At the concentration of 1 μmol L^{-1}, ΔI reached the maximum value, indicating that the loading of ZEN aptamer chain on Au NPs@Ce-TpBpy COF reached the maximum value. Therefore, in the follow-up study, 1 μmol L^{-1} was selected as the optimal ZEN aptamer chain concentration.

Effect of incubation time of ZEN aptamer on the response current

The ZEN aptamer incubation time is another important factor affecting the sensitivity of the sensor, which affects the amount of binding to gold nanoparticles. Other experimental conditions were fixed unchanged, the pH of the buffer was kept at 7.0, the ZEN incubation time was 100 min, and the ZEN aptamer chain concentration was 1 μmol L^{-1}. When the incubation time of ZEN aptamer were 20 min, 40 min, 60 min, 80 min, 100 min, 120 min, the change value ΔI of the response current was measured. The results are shown in Fig. 8D. With the prolongation of incubation time, the change value of the current response reached the maximum value at 100 min of incubation, indicating that the binding of ZEN aptamer to gold nanoparticles reached the maximum value at this time. Therefore, in the follow-up study, the optimal ZEN aptamer incubation time was selected as 100 min.

Effect of the applied potential

The effect of the applied potential on the biosensor response was provided in ESI, S1.† With the decreasing potential from −0.3 V to −0.7 V, the response of the biosensor increased significantly. To avoid interference at high negative applied potential, a potential of −0.6 V (*vs.* SCE) was selected as the applied potential for amperometric measurements.

The detection performance of aptamer sensor for ZEN

Under the optimized conditions, the response current of the ZEN aptasensor to different concentrations of ZEN toxin is measured (Fig. 9). In the range of 0.001 ng mL^{-1}–10.0 ng mL^{-1}, the response current (ΔI) of the aptamer sensor showed a good linear relationship with the logarithm of ZEN toxin concentration. The linear equation is $\Delta I = 0.401 \lg c + 1.948$, ($R^2 = 0.9906$) and the detection limit of ZEN is 0.389 pg mL^{-1} (at 3σ). Compared with previously reported methods for ZEN (Table 1), this strategy has satisfactory sensitivity and linear range, which can meet the needs of real sample detection.

Selectivity of aptamer sensor

Whether the aptasensor has practical application value is closely related to whether it has good selectivity. In this experiment, the interference of five common food toxins on aptamer sensors was investigated. The selectivity of sensors were investigated for 20 ng mL^{-1} of ochratoxin A (OTA), 20 ng mL^{-1} of ochratoxin B (OTB), 20 ng mL^{-1} of aflatoxin B1 (AFB_1), 20 ng mL^{-1} of aflatoxin B_2 (AFB_2), 20 ng mL^{-1} of fumonisins, and 2 ng mL^{-1} of ZEN (interference concentration 10 times higher than ZEN concentration). Firstly, the response current value ΔI of each of the above substances was measured by the separate solution method, and then the response current value ΔI when ZEN was mixed with each interfering substance in a volume ratio of 1 : 1 was measured by the mixed solution method. The detection results are shown in Fig. 10. The five interfering substances have little interference to the aptamer sensor,

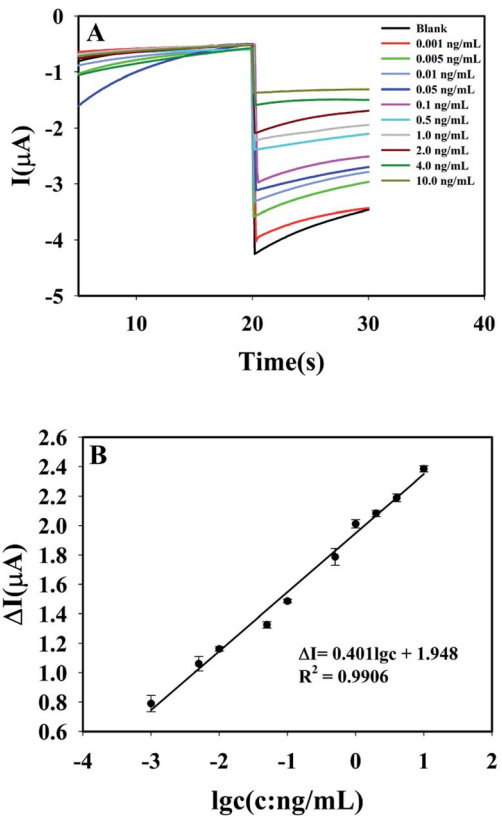

Fig. 9 *I*–*t* curves (A) and calibration curve (B) of aptamer sensor for different ZEN concentrations (0.001 ng mL^{-1}, 0.005 ng mL^{-1}, 0.01 ng mL^{-1}, 0.05 ng mL^{-1}, 0.1 ng mL^{-1}, 0.5 ng mL^{-1}, 1.0 ng mL^{-1}, 2.0 ng mL^{-1}, 4.0 ng mL^{-1} and 10.0 ng mL^{-1}).

Table 1 A comparison of the proposed method with other methods for the detection of ZEN

Method	Linear range	LOD	Ref.
Colloidal gold immunochromatographic	50–800 ng g^{-1}	44.3 ng g^{-1}	27
HPLC	0.05–100 ng mL^{-1}	0.02 ng mL^{-1}	28
Assay using attenuated internal reflection	0.01–1000 ng mL^{-1}	0.08 ng mL^{-1}	29
Aptamer-based ratiometric fluorescent nanoprobe	31.4–628 nmol L^{-1}	7.5 nmol L^{-1}	30
Silica nanoparticle-based fluorescence aptasensor	0.005–150 ng mL^{-1}	0.012 ng mL^{-1}	31
Lateral flow immunoassay based on Au@PDA	0.01–50 ng mL^{-1}	7.4 pg mL^{-1}	32
Au NPs@ Ce-TpBpy COF portable biosensor	0.001–10.0 ng mL^{-1}	0.389 pg mL^{-1}	This work

indicating that the aptasensor proposed by this method has good selectivity and anti-interference ability.

Reproducibility

In order to investigate the reproducibility of the aptamer sensor, 5 electrodes were used to prepare the sensor separately and measure 5 ng mL^{-1} ZEN in this experiment. Each electrode was measured three times in parallel. The measurement results are shown in Fig. 11. The relative standard deviation (RSD) was 5.04% ($n = 5$), which shows that the aptamer sensor has good reproducibility.

Comparison with other methods

The proposed detection method is compared with some other common detection methods for ZEN (Table 1). This method has a wide detection range, low detection limit, simple operation, no need for sophisticated instruments, is convenient and fast, and can meet the needs for detection on the spot.

Practical application is one of the important standards to investigate the application value of the adaptive sensor. Enzyme-linked immunosorbent assay kit adopts one-step sandwich method using HRP labeled antibody to catalyze the H_2O_2 oxidizing TMB and changing to blue color, and the target concentration is determined according to its absorbance at 450 nm. Firstly, the performance of the ELISA kit is determined and the results are shown in Fig. 12. Within the test range of 0.25 ng mL^{-1}–8 ng mL^{-1}, the absorbance obtained by the ELISA kit has a good linear relationship with the logarithm of ZEN toxin concentration. The linear equation is Abs = 0.6519 lg c + 0.4156, and the linear correlation coefficient R^2 = 0.9921 with the detection limit of 0.083 ng mL^{-1} (at 3σ).

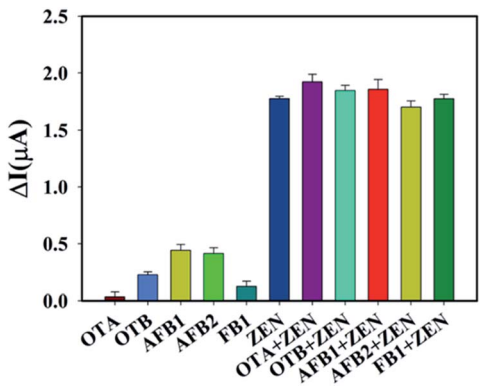

Fig. 10 Selectivity of aptamer sensor.

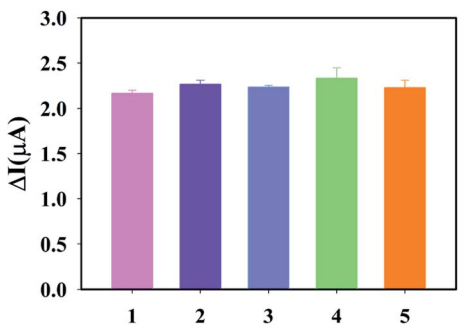

Fig. 11 Reproducibility of aptamer sensor.

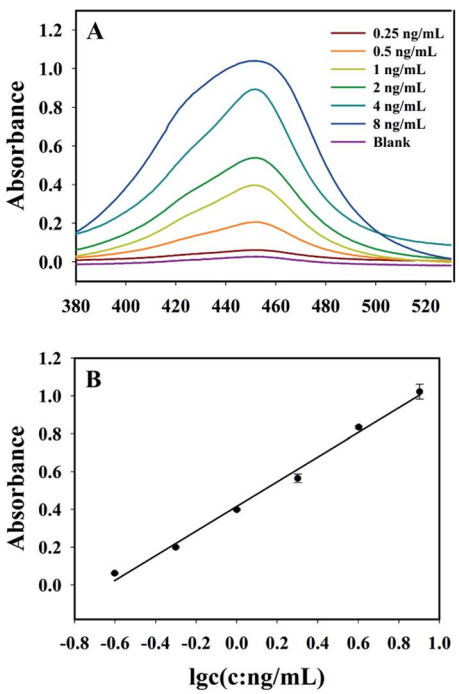

Fig. 12 The absorption curves (A) and calibration curve (B) of the ELISA kit.

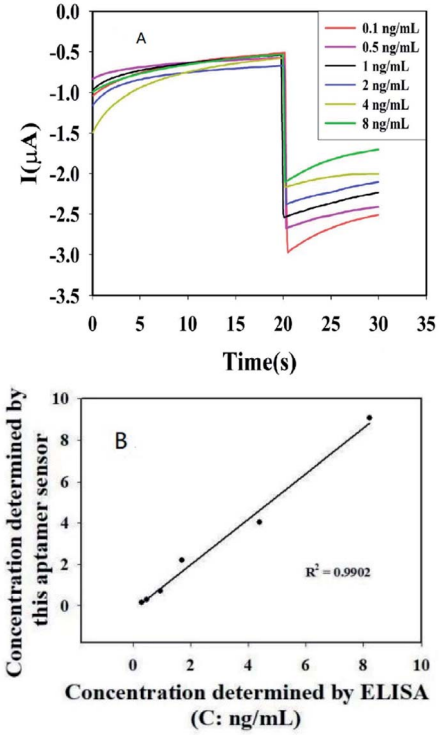

Fig. 13 *I*–*t* curves measured in cornflour stored (A) and the calibration curve of ZEN aptamer sensor and ELISA for the measurement results of different concentrations of ZEN determination results (B).

In this experiment, cornmeal was used as the detection sample, and ZEN cannot be detected by both ELISA Kit and ZEN aptamer sensor because the content is lower than the detection limit. In order to test the accuracy of the ZEN aptamer sensor, these two methods were used to simultaneously detect six standard solution with different concentration of ZEN added in extraction of cornflour stored. Catalytic current *vs.* time for the cornflour stored has been shown in Fig. 13A and the correlation of the results is shown in Fig. 13B. There is a good linear relationship between the two methods for the same concentration of ZEN, and the linear correlation coefficient $R^2 = 0.9902$, which proves that the proposed ZEN aptamer sensor has reliable accuracy and can be used in practical applications.

Table 2 Determination of ZEN recovery

Sample	Added (ng mL^{-1})	Found (ng mL^{-1})	RSD (%)	Recovery (%)
1	0.0	No found		
2	1.0	1.02	5.54	102.0
		1.03		103.0
		0.93		93.0
3	5.0	5.02	1.26	100.4
		5.12		102.4
		5.14		102.8
4	10.0	10.47	4.10	104.7
		9.77		97.7
		9.75		97.5

Recovery analysis

To verify the feasibility of this method in real sample detection, it is used to study the recovery of ZEN in crops. Before detection, the samples were pretreated as mentioned in the experimental part. Then, standard solutions are added into the real samples at different levels (1 ng mL^{-1}, 5 ng mL^{-1}, and 10.0 ng mL^{-1}) their concentrations are determined using the proposed aptamer sensor under the optimized conditions. The determination results are shown in Table 2. The recovery ranges from 93.0% to 104.7%.

Conclusions

In this work, an aptasensor for the quantitative detection of zearalenone based on a U-disk electrochemical workstation is developed. Through the modification of TpBpy COF with cerium element, a nano-mimetic enzyme Ce-TpBpy COF was prepared, which has good catalytic activity to H_2O_2. The catalytic current for the reduction of hydrogen peroxide is measured by chronoamperometry in Tris acetic acid buffer solution (pH 7.0). In the range of 0.001 ng mL^{-1}–10.0 ng mL^{-1}, the response current ΔI shows a good linear relationship with the logarithm of ZEN toxin concentration, and the detection limit is 0.389 pg mL^{-1} (at 3σ). The proposed detection method has good selectivity and high sensitivity, which can be used for the rapid and low-cost detection of ZEN in the field.

Conflicts of interest

The authors declare there are no conflicts of interest regarding the publication of this paper.

Acknowledgements

This work was supported by the National Natural Science Foundation of China (Grant No. 21765026).

References

1 H. Kakeya, N. Takahashi-Ando, M. Kimura, R. Onose, I. Yamaguchi and H. Osada, *Biosci., Biotechnol., Biochem.*, 2014, **66**(12), 2723–2726.
2 C. Juan, A. Ritieni and J. Mañes, *Food Chem.*, 2012, **134**(4), 2389–2397.
3 K. Jiang, D. Nie, Q. Huang, K. Fan, Z. Tang, Y. Wu and Z. Han, *Biosens. Bioelectron.*, 2019, **130**, 322–329.
4 A. M. Khaneghah, L. M. Martins, A. M. Von Hertwig, R. Bertoldo and A. S. Sant'Ana, *Trends Food Sci. Technol.*, 2018, **71**, 13–24.
5 A. Rogowska, P. Pomastowski, G. Sagandykova and B. Buszewski, *Toxicon*, 2019, **162**, 46–56.
6 J. R. Aldana, L. J. G. Silva, A. Pena, J. Mañes V and C. M. Lino, *Food Control*, 2014, **45**, 51–55.
7 G. Cai, S. Pan, N. Feng, H. Zou, J. Gu, Y. Yuan, X. Liu, Z. Liu and J. Bian, *Ecotoxicol. Environ. Saf.*, 2019, **175**, 263–271.

8 Z. Wu, E. Xu, M. F. J. Chughtai, Z. Jin and J. Irudayaraj, *Food Chem.*, 2017, **230**, 673–680.
9 X. Ji, C. Yu, Y. Wen, J. Chen, Y. Yu, C. Zhang, R. Gao, X. Mu and J. He, *Biosens. Bioelectron.*, 2019, **129**, 139–146.
10 Z. Huang, J. He, Y. Li, C. Wu, L. You, H. Wei, K. Li and S. Zhang, *J. Chromatogr. A*, 2019, **1602**, 11–18.
11 W. Hu, X. Li, G. He, Z. Zhang, X. Zheng, P. Li and C. M. Li, *Biosens. Bioelectron.*, 2013, **50**, 338–344.
12 I. Slobodchikova and D. Vuckovic, *J. Chromatogr. A*, 2018, **1548**, 51–63.
13 B. He and X. Yan, *Sens. Actuators, B*, 2019, **306**, 127558.
14 S. Ghayyem, A. Swaidan, A. Barras, M. Dolci and F. Faridbod, *Talanta*, 2021, **226**, 122082.
15 X. Shu, Y. Chang, H. Wen, X. Yao and Y. Wang, *RSC Adv.*, 2020, **10**(25), 14953–14957.
16 E. Pourtaheri, M. A. Taher, G. A. M. Ali, S. Agarwal and V. K. Gupta, *J. Mol. Liq.*, 2019, **289**, 111141.
17 E. L. Teo, G. Ali, H. Algarni, W. Cheewasedtham, T. Rujiralai and K. F. Chong, *Mater. Chem. Phys.*, 2019, **231**, 286–291.
18 J. Xin, Y. Zhou, X. Wang, G. Xu, M. Xie, L. Liu, R. Zhao, Y. Wu and M. Wang, *Food Chem.*, 2021, **347**, 129075.
19 J. Cui, L. Kan, Z. Li, L. Yang, M. Wang, L. He, Y. Lou, Y. Xue and Z. Zhang, *Talanta*, 2021, **228**, 122060.
20 L. Wang, Y. Yang, H. Liang, N. Wu, X. Peng, L. Wang and Y. Song, *J. Hazard Mater.*, 2021, **409**, 124528.
21 W. Gao, G. Li, H. Liu, Y. Tian, W. T. Li, Y. Fa, Y. Cai, Z. Zhao, Y. L. Yu, G. Qu and G. Jiang, *Sci. Total Environ.*, 2021, **764**, 144388.
22 D. B. Shinde, H. B. Aiyappa, M. Bhadra, B. P. Biswal, P. Wadge, S. Kandambeth, B. Garai, T. Kundu, S. Kurungot and R. Banerjee, *J. Mater. Chem. A*, 2016, **4**(7), 2682–2690.
23 S. Y. Li, S. Meng, X. Q. Zou, M. El-Roz, I. Telegeev, O. Thili, T. X. Liu and G. S. Zhu, *Microporous Mesoporous Mater.*, 2019, **285**, 195–201.
24 X. Chen, Y. Huang, N. Duan, S. Wu, X. Ma, Y. Xia, C. Zhu and Z. Wang, *Anal. Bioanal. Chem.*, 2013, **405**(20), 6573–6581.
25 G. Frens, *Nature (London), Phys. Sci.*, 1973, **241**(105), 20–22.
26 Y. J. Hou, N. Long, B. Y. Jia, X. F. Liao, M. H. Yang, L. Z. Fu, L. D. Zhou, P. Sheng and W. J. Kong, *Food Control*, 2022, **135**, 108833.
27 X. Mao, Y. Wu, H. Chen, Y. Wang, B. Yu and G. Shi, *Anal. Methods*, 2020, **12**(46), 5628–5634.
28 J. Xu, T. Liu, J. Chi, W. Zhang and Z. Xie, *Talanta*, 2020, **219**, 121309.
29 M. O. Caglayan and Z. Stünda, *Food Chem. Toxicol.*, 2020, **136**, 111081.
30 X. Tan, X. Wang, A. Hao, Y. Liu and D. Ming, *Microchem. J.*, 2020, **157**, 104943.
31 H. Tan, T. Guo, H. Zhou, H. Dai and L. Ma, *Anal. Bioanal. Chem.*, 2020, **412**(23), 5627–5635.
32 S. Xu, G. Zhang, B. Fang, Q. Xiong and W. Lai, *ACS Appl. Mater. Interfaces*, 2019, **11**(34), 31283–31290.